*J Mater Sci* (2020) 55:7870–7882

Materials for life sciences

# Effect of $Mg^{2+}$ on porous $Mg_xCa_{3-x}(PO_4)_2$ composite scaffolds for bone engineering by 3D gel-printing

Huiping Shao[1,*], Yumeng Zhang[1], Tao Lin[1], Jiang Peng[2,3], Aiyuan Wang[2,3], Fucheng Yu[4], Zhinan Zhang[1], and Luhui Wang[1]

[1] Institute for Advanced Materials and Technology, University of Science and Technology Beijing, Beijing 100083, China
[2] Institute of Orthopedics, Chinese PLA General Hospital, Beijing 100853, China
[3] Key Laboratory of Regenerative Medicine in Orthopedics, Key Laboratory of Musculoskeletal Trauma & War Injuries PLA, Beijing 100853, China
[4] School of Material Science and Engineering, Lanzhou University of Technology, Lanzhou, China

**Received:** 20 October 2019
**Accepted:** 19 March 2020
**Published online:** 27 March 2020



## ABSTRACT

In this paper, the precursors of $Mg_xCa_{3-x}(PO_4)_2$ powders with different magnesium contents were first synthesized by a liquid-phase precipitation method with simple operation and easy control of the reaction process. And the $Mg_xCa_{3-x}(PO_4)_2$ slurry was used to print porous scaffolds by 3D gel-printing (3DGP), and then the scaffolds were degreased and sintered to improve performance, which simplifies the process and saves costs. The effects of different magnesium ions ($Mg^{2+}$) doping contents on the precursors were investigated. When $Mg^{2+}$ doping content is 0, 5 mol%, 10 mol% and 30 mol%, the particle diameters of the precursors are, respectively, 44.51 μm, 41.91 μm, 38.38 μm and 31.93 μm. The effects of different $Mg^{2+}$ doping amounts on the biological and mechanical properties of the scaffolds were studied. When the doping $Mg^{2+}$ content is 0, 5 mol%, 10 mol% and 30 mol%, respectively, the porosity of the scaffolds is 72.11%, 70.26%, 69.83% and 65.15%, and the strength is 1.04 ± 0.01 MPa, 0.73 ± 0.17 MPa, 0.23 ± 0.01 MPa and 1.89 ± 0.21 MPa, respectively. The degradation behavior was observed when the scaffolds were immersed in phosphate buffer saline for 8 weeks, which indicate that $Mg_xCa_{3-x}(PO_4)_2$ composite scaffolds are expected to be more widely used in the field of bone defect repairing.

## Introduction

At present, due to the difficulty in reconstructing large bone segments, large load-bearing bone defects after trauma, infection or tumor resection are still the main problems faced by surgeons [1–3]. The challenge in the field of porous scaffolds is to develop a product that matches the biomechanical properties of bone and also has sufficient biological activity to stimulate new bone regeneration [4–6]. Due to the

Huiping Shao and Yumeng Zhang have contributed equally.

Address correspondence to E-mail: shaohp@ustb.edu.cn



https://doi.org/10.1007/s10853-020-04590-x

need for effective and comprehensive repairing of bone defects, bioactive ceramics and their composites are moving toward high mechanical strength, good bioactivity and controlled biodegradation [7, 8].

β-tricalcium phosphate (β-TCP) has been considered a valuable implant material for many years [9–11]. In fact, β-TCP has a good potential application in bone defects due to its good human compatibility and chemical composition similar to the organic composition of bone [12]. As a bio-absorbable material, β-TCP bio-ceramics are considered to be an ideal temporary scaffold in bone tissue engineering. It will promote the initial formation of new bone tissue and eventually be replaced by new bone [13]. In order to further improve the application characteristics of β-TCP in tissue engineering, people are now paying attention to the improved synthetic calcium phosphate, which changes its physical and chemical properties and biological properties by ion doping [14–19]. Mg is the abundant cation in the human body and ranks fourth. It is present in calcified living tissues (about 0.5% in bone and enamel, and more than 1% in dentin). The lack of Mg in bones has been considered to be one of the causes of osteoporosis [20]. When part of $Ca^{2+}$ in β-TCP is replaced by $Mg^{2+}$, the rate of degradation of the porous scaffolds in vivo can be regulated [21]. There are many methods for preparing composite calcium phosphate bioceramics, such as solid-phase reaction, sol–gel technique, microwave synthesis method and liquid-phase precipitation method [22–26]. The liquid-phase precipitation method is simple in process and low reaction temperature. Therefore, it is one of the most commonly used methods. In this study, $Mg_xCa_{3-x}(PO_4)_2$ composite ceramics are expected to be used in preparing specific porous scaffolds for enhanced large-area segmental bone defect regeneration and in situ repair.

There are many methods for preparing porous bioceramic scaffolds, such as solvent casting and particle leaching, combination of direct foaming and sacrificial template methods and 3D printing [27–29]. Although the traditional method can also prepare porous bone repair materials, there are some defects: for example, the pores in the material are not coherent, the pore diameter cannot be accurately controlled, and the shape of the pores is single. Therefore, researchers began to study the application of 3D printing technology in the preparation of porous scaffolds. The combination of 3D printing technology and bone tissue engineering scaffolds can improve the osteogenic performance of the graft, reduce the amount of autologous bone and effectively solve the problem of insufficient bone graft in clinical practice. The cancellous bone of the human body is a porous structure, which is arranged by intertwined bone trabeculae and is distributed inside the bone. 3DGP is a rapid prototyping technology based on the gel-molding process. It is a new type of rapid prototyping technology that can be "tailored" and can also print the simulated trabecular micropores to promote bone growth and healing [30, 31]. The slurry is extruded from the nozzle of the printer by gas pressure, and the layer material is scanned and processed in two dimensions under the computer control using the geometric information determined by the CAD model of the part. From the point to the line, from the line to the surface and from the surface to the body, the layers are stacked to obtain a three-dimensional stent blank, and then the body is dried and sintered to obtain the desired stent [32].

In the paper, the effect of $Mg^{2+}$ on $Mg_xCa_{3-x}(PO_4)_2$ composite scaffolds and preparation process and powder characteristics of $Mg_xCa_{3-x}(PO_4)_2$ composite powders were studied. The influence of different $Mg^{2+}$ doping contents (0, 5 mol%, 10 mol% and 30 mol%) on degradability and mechanical properties of β-TCP scaffolds was analyzed. The research results show that the proper doping of $Mg^{2+}$ is helpful for the preparation of $Mg_xCa_{3-x}(PO_4)_2$ scaffold with good mechanical properties and degradability for the repair of cancellous bone.

## Experimental

Firstly, $Mg_xCa_{3-x}(PO_4)_2$ powders with different magnesium contents were synthesized by a simple liquid-phase precipitation method, and then the $Mg_xCa_{3-x}(PO_4)_2$ slurry for printing is prepared. Next, the $Mg_xCa_{3-x}(PO_4)_2$ porous scaffolds were printed by 3DGP, and then the scaffolds were degreased and sintered. Finally, the $Mg_xCa_{3-x}(PO_4)_2$ scaffolds were tested.

### Materials

The materials used in this study are as follows: diammonium phosphate (AR, Sinopharm Chemical Reagent Co., Ltd), calcium chloride (AR, Sinopharm

Chemical Reagent Co., Ltd), magnesium chloride hexahydrate(AR, Sinopharm Chemical Reagent Co., Ltd), ammonia (AR, Sinopharm Chemical Reagent Co., Ltd), acrylamide monomer (AR, Tianjin GuangFu Fine Chemicals), *N*,*N*′-methylenebisacrylamide (AR, Sinopharm Chemical Reagent Co., Ltd),ammonium citrate (AR, Beijing Yili Fine Chemicals), PVA (AR, Jiangxi Alpha Gaoke Pharmaceutical Co., Ltd), oleic acid (AR, Shandong West Asia Chemical Co., Ltd), citric acid (AR, Sinopharm Chemical Reagent Co., Ltd) and deionized water (University of Science and Technology Beijing). The characteristics of the materials used in this study are shown in Table 1.

## Preparation of $Mg_xCa_{3-x}(PO_4)_2$ powders

Figure 1 shows the preparation process of $Mg_xCa_{3-x}(PO_4)_2$ powders for 3DGP. Different $Mg^{2+}$ doping contents (0, 5 mol%, 10 mol% and 30 mol%) of $Mg_xCa_{3-x}(PO_4)_2$ precursor powders were synthesized by liquid-phase precipitation. Anhydrous calcium chloride ($CaCl_2$), diammonium hydrogen phosphate ($(NH_4)_2HPO_4$) and magnesium chloride hexahydrate ($MgCl_2{\cdot}6H_2O$) were used as starting chemical precursors for magnesium calcium phosphate ($Mg_xCa_{3-x}(PO_4)_2$). When Ca/P ratio is 3.5,the β-TCP scaffolds were obtained by sintering at 1100 °C for 3 h. In order to replace some of calcium ions ($Ca^{2+}$) in β-TCP with $Mg^{2+}$, an appropriate amount of $MgCl_2{\cdot}6H_2O$ was dissolved slowly in $CaCl_2$ and $(NH_4)_2HPO_4$ mixed solution to achieve a predetermined (Ca + Mg)/P molar ratio of 3.5 [22], and $Mg^{2+}/(Ca^{2+}+Mg^{2+})$ molar ratio was 0, 5, 10 and 30, respectively. The pH value of mixed solution was adjusted to be about 5.0–6.0 by aqueous ammonia. After the addition was completed, the mixture was stirred at a constant rate and reacted at 40 °C for 2 h. The reacted solution was allowed to settle for 24 h, and the precipitate was separated by filtration and dried at 80 °C. The dried precipitate was studied and printed for scaffolds.

## Slurry preparation and characterization

The representative slurry formulations of $Mg_xCa_{3-x}(PO_4)_2$ scaffolds are shown in Table 2. When the molar ratio of (Ca + Mg)/P is 3.5, and the molar ratio of $Mg^{2+}/(Ca^2 + Mg^{2+})$ in the four groups of samples is 0, 5, 10 and 30, respectively, the corresponding X in $Mg_xCa_{3-x}(PO_4)_2$ is 0, 0.15, 0.3 and 0.9. The last two columns are the amount of $Mg_xCa_{3-x}(PO_4)_2$ precursor powder that can be uniformly dispersed in the 3 g premixed solution. $Mg_xCa_{3-x}(PO_4)_2$ composite powders were mixed with premixed solution which was stirred by an appropriate amount of acrylamide, *N*,*N*′-methylenebisacrylamide, ammonium citrate and PVA. An appropriate amount of oleic acid can be added to make the slurry more evenly dispersed [22].

## Preparation of $Mg_xCa_{3-x}(PO_4)_2$ scaffolds

Table 3 shows the printing parameters of 3DGP for porous $Mg_xCa_{3-x}(PO_4)_2$ scaffolds. The size of the experimental design bracket is 15 mm × 15 mm × 8 mm. The large hole size of the bracket is 1.5 mm × 1.5 mm × 1.5 mm, and the diameter of the needle used for printing is 0.2 mm. From this calculation, it

**Table 1** Characteristics of materials used in this study

| Materials | Purity | Density | Boiling point/°C | Manufacturer |
|---|---|---|---|---|
| Diammonium phosphate | AR | 1.62 | – | Sinopharm Chemical Reagent Co., Ltd |
| Calcium chloride | AR | 1.09 | – | Sinopharm Chemical Reagent Co., Ltd |
| Magnesium chloride hexahydrate | AR | 1.57 | – | Sinopharm Chemical Reagent Co., Ltd |
| Ammonia | AR | 0.91 | 38 | Sinopharm Chemical Reagent Co., Ltd |
| Acrylamide monomer | AR | 1.32 | – | Tianjin GuangFu Fine Chemicals |
| *N*,*N*′-methylenebisacrylamide | AR | 1.23 | – | Sinopharm Chemical Reagent Co., Ltd |
| Ammonium citrate | AR | 1.22 | – | Beijing Yili Fine Chemicals |
| PVA | AR | 1.27 | – | Jiangxi Alpha Gaoke Pharmaceutical Co., Ltd |
| Oleic acid | AR | 0.89 | 360 | Shandong West Asia Chemical Co., Ltd |
| Citric acid | AR | 1.67 | – | Sinopharm Chemical Reagent Co., Ltd |
| Deionized water | – | 1.0 | 100 | University of Science and Technology Beijing |

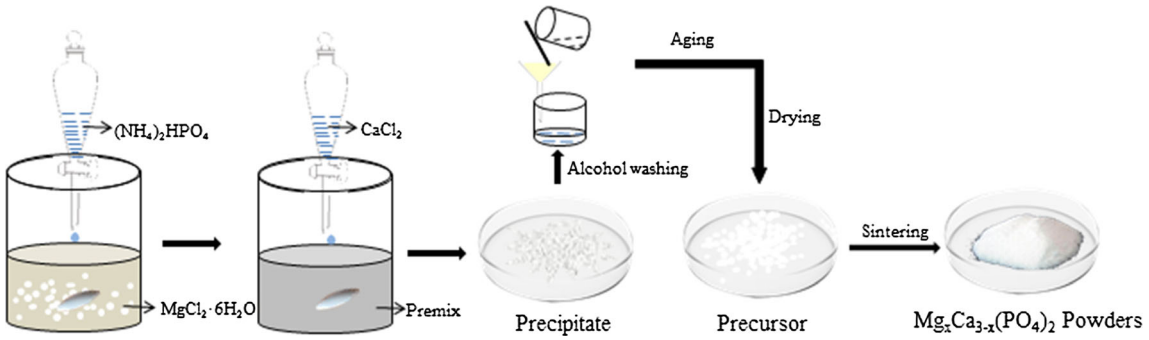


**Figure 1** The preparation process of $Mg_xCa_{3-x}(PO_4)_2$ powders for 3DGP [22].

**Table 2** Chemical composition of $Mg_xCa_{3-x}(PO_4)_2$ ceramic slurry

| Samples | (Ca + Mg)/P (mol%) | $Mg^{2+}/(Ca^{2+}+Mg^{2+})$ (mol%) | $x$ | Product | $Mg_xCa_{3-x}(PO_4)_2$ (g) | Premixed solution (g) |
|---|---|---|---|---|---|---|
| TCP-0 Mg | 3.5 | 0 | 0 | $Ca_3(PO_4)_2$ | 2.67 | 3 |
| TCP-5 Mg | 3.5 | 5 | 0.15 | $Mg_{0.15}Ca_{2.85}(PO_4)_2$ | 3.81 | 3 |
| TCP-10 Mg | 3.5 | 10 | 0.3 | $Mg_{0.3}Ca_{2.7}(PO_4)_2$ | 3.16 | 3 |
| TCP-30 Mg | 3.5 | 30 | 0.9 | $Mg_{0.9}Ca_{2.1}(PO_4)_2$ | 2.50 | 3 |

**Table 3** Printing parameters of 3DGP for porous $Mg_xCa_{3-x}(PO_4)_2$ scaffolds

| Printing parameters | Nozzle diameter (mm) | Layer height (mm) | Printing speed (mm/s) | Pressure (MPa) |
|---|---|---|---|---|
| Value | 0.2 | 0.12 | 6 | 0.35 |

can be known that the porosity of the bracket is about 61%. The UG software is used to design a cube and save it as an STL file, and 2D and 3D printing diagram of the scaffolds is shown in Fig. 2. The file is imported into the matching printing layering software, and the inside of the cube is uniformly distributed with a rectangular body structure. After the G-code is generated, the stand is printed with 3D gel-printing device. And remove it after the stand is sufficiently dry. The temperature was raised to 1100 °C at 2 °C/min in a high-temperature pipe furnace (BFG-12A), kept for 3 h, and cooled to room temperature.

## Performance Testing

The phase composition of the scaffolds sintered at 1100 °C was verified by X-ray diffraction (XRD; SmartLab) at 40 kV/40 mA. Scanning electron microscopy (SEM; Zeiss EVO18) was used to observe the surface morphology of the C-coated powder and scaffold at an accelerating voltage of 10 kV. The scaffolds porosity was measured by the drainage method [33, 34]:

$$P = (W_2 - W_1)/(W_2 - W_3) \times 100\% \quad (1)$$

where $P$ is the porosity of the stent, $W_1$ is the dry weight of the stent, $W_2$ is the weight of the stent saturated with water and $W_3$ is the weight of the stent suspended in the water. Five samples were tested to calculate the average porosity. Mechanical testing was performed using a static mechanical tester (SUST-CMT5605) and a 10 kN load cell. And the samples were tested at a constant crosshead displacement rate of 0.5 mm/min.

To evaluate the biodegradability of the scaffolds, the PBS buffer having an initial pH value of 7.4 was used with an S/L ratio of 1.0 g/200 ml. At the predetermined time period, the scaffold was rinsed with ethanol, dried at 80 °C for 12 h and weighed (Wt) to determine the mass change of the scaffold and pH change of the solution.

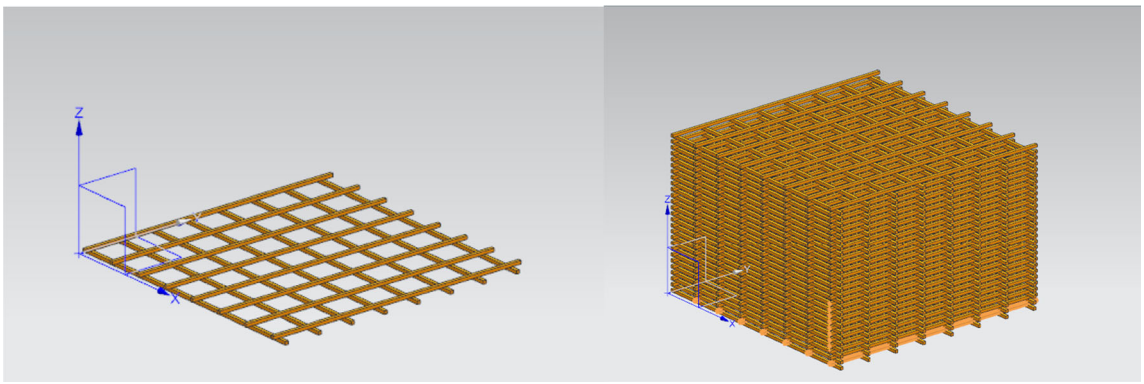

**Figure 2** Print path generated by the UG software.

$$W = W_0 - W_t/W_0 \times 100\% \quad (2)$$

where $W_0$ is the initial weight of the scaffold and $W_t$ is the weight of the scaffold for different soaking times [35].

## Results and discussion

The morphology and particle size distribution of $Mg_xCa_{3-x}(PO_4)_2$ powders were important because they directly affect the performance of the printing slurry and also directly affect the performance of the printing scaffolds. In this part, the morphology and particle size distribution of $Mg_xCa_{3-x}(PO_4)_2$ powder, the rheological properties of the slurry, mechanical properties and degradation performance of the printing scaffolds were discussed.

### Characteristics of $Mg_xCa_{3-x}(PO_4)_2$ powders

The $Mg_xCa_{3-x}(PO_4)_2$ powders are characterized by SEM, EDX and XRD. Figure 3 shows that SEM images and particle size distribution of $Mg_xCa_{3-x}(PO_4)_2$ precursor powders prepared in this study. When $Mg^{2+}$ doping content is 0, 5 mol%, 10 mol% and 30 mol%, the particle size of the precursors are about 44.51 μm, 41.91 μm, 38.38 μm and 31.93 μm, respectively. The particle size of the powder is suitable for 3D printing. As shown in Fig. 3, the powders have an irregular shape and a certain agglomeration phenomenon. The agglomeration of ceramic powders during the drying process is due to the existence of the solid–liquid interface and the surface tension of the liquid. The collapse of gel pores and the accumulation of particles can easily occur. After the addition of $Mg^{2+}$, the agglomeration of the powder is improved that attributes to the stability of β-TCP structure. $Mg^{2+}$ can be present as a stabilizer in $Mg_xCa_{3-x}(PO_4)_2$.

The purpose of EDX spectrum analysis is to verify whether $Mg^{2+}$ participate in the reaction and form a composite phase. As shown in Fig. 4,EDX spectrum analysis revealed the presence of oxygen (O), calcium (Ca), phosphorus (P) and a small amount of Mg. Mg element was detected in $Mg_xCa_{3-x}(PO_4)_2$ precursor powders prepared in this study. $Mg^{2+}$ was successfully doped into β-TCP powders by liquid-phase precipitation. The magnesium-doped composite powder has the same elemental composition, but the content of each element is different. As $Mg^{2+}$ content increases, the peak of Mg element is also more pronounced. Figure 5 shows XRD pattern of different $Mg^{2+}$ content powders after sintering. When $Mg^{2+}$ content is different, XRD diffraction peaks of the powders are consistent with the standard peak of β-TCP (PDF#09-0169). XRD diffraction pattern of the powders and EDX analysis confirmed that when $Mg^{2+}$ replaced a part of $Ca^{2+}$ in β-TCP, a crystallized $Mg_xCa_{3-x}(PO_4)_2$ phase was formed.

### Rheological properties of slurry

Figure 6 shows the apparent viscosity of slurry with different $Mg^{2+}$ contents. At a solid content of 50 vol% [22], the slurry viscosity decreases with increasing shear rate, exhibiting the characteristics of a pseudoplastic fluid. Since the colloidal particles in the slurry belong to a chain polymer, when the shear rate is low, the long-chain molecules are entangled with each other, and the viscosity of the slurry is large. As the shear rate increases, the long-chain polymer shrinks, and the viscosity decreases with the shear stress.

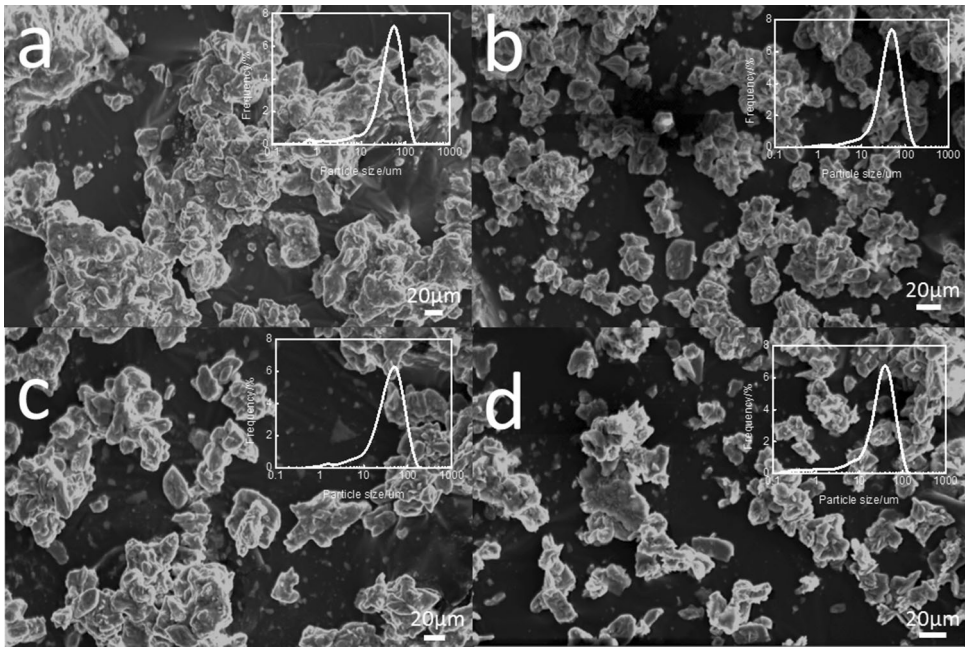


**Figure 3** SEM images and particle size distribution of precursor powders for 3DGP: **a** TCP-0 Mg, **b** TCP-5 Mg, **c** TCP-10 Mg and **d** TCP-30 Mg.

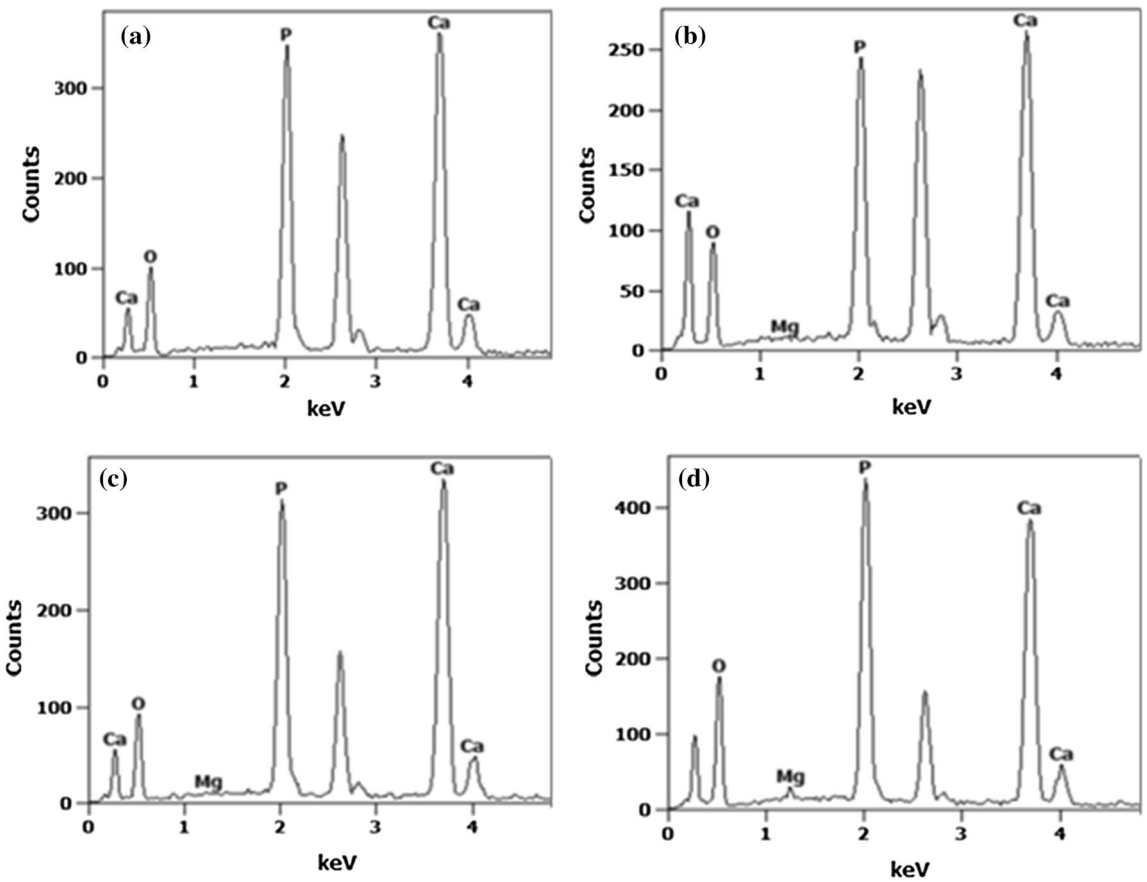


**Figure 4** EDX component analysis of $Mg_xCa_{3-x}(PO_4)_2$ precursor powders for 3DGP: **a** TCP-0 Mg, **b** TCP-5 Mg, **c** TCP-10 Mg and **d** TCP-30 Mg.

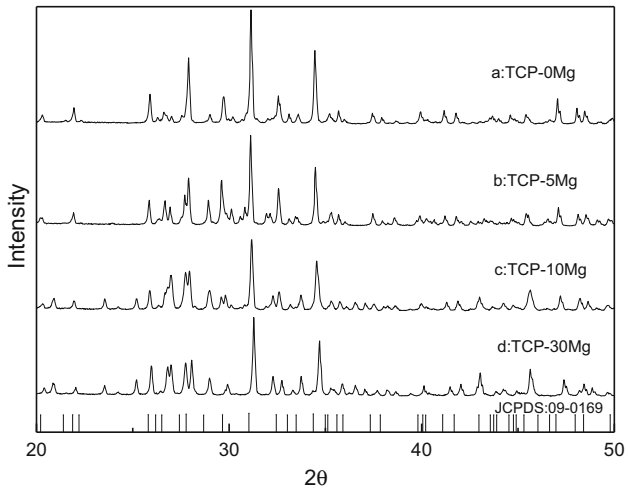


**Figure 5** XRD pattern of $Mg_xCa_{3-x}(PO_4)_2$ powders after sintering: **a** TCP-0 Mg [22], **b** TCP-5 Mg, **c** TCP-10 Mg and **d** TCP-30 Mg.

When the $Mg^{2+}$ content is different, the viscosity of the slurry changes, and the viscosity gradually decreases as the shear rate increases. When the shear rate is less than 160 $s^{-1}$, the viscosity of TCP-30 Mg slurry is higher than TCP-10 Mg at the same shear rate. When the shear rate is greater than 160 $s^{-1}$, the viscosity of the two is close, and the viscosity of TCP-30 Mg is slightly lower.

## Characteristics of $Mg_xCa_{3-x}(PO_4)_2$ scaffolds

The scaffolds for tissue engineering applications are expected to have porous structures with pore interconnect. The porous structure enables cells to attach better to the scaffold, facilitating cell proliferation and

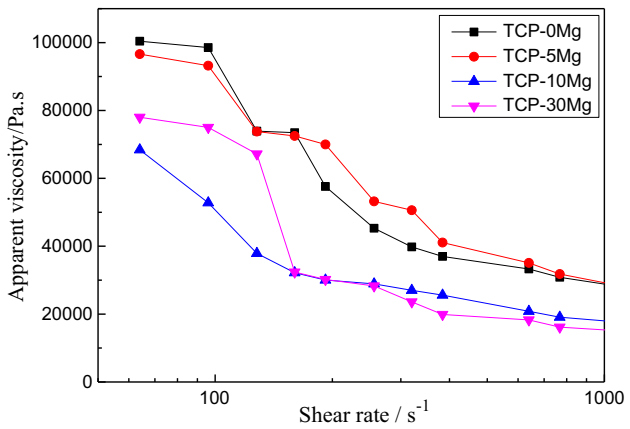


**Figure 6** The apparent viscosity of $Mg_xCa_{3-x}(PO_4)_2$ slurry with different $Mg^{2+}$ contents at different shear rates.

internal growth of new tissues and transport of nutrients to developing bones. The macro view of the $Mg_xCa_{3-x}(PO_4)_2$ scaffolds is shown in Fig. 7. The addition of $Mg^{2+}$ has no obvious effect on the macroscopic morphology of the green body stent, and the stent shows good formability. As the $Mg^{2+}$ content increases, the contraction of the stent also gradually increases after sintering. From Fig. 7($d_1$–$d_4$), it can be seen that when the magnesium content is 30 mol%, the stent has obvious contraction. And the stent has a slight phenomenon of warping around the periphery.

Figure 8 shows the shape integrity, and surface morphology of $Mg_xCa_{3-x}(PO_4)_2$ porous scaffolds printed by 3DGP were investigated by SEM. As shown in Fig. 8$a_1$–$d_1$, the surface of the printed silk is smooth, and the macroscopic pores of the stent exhibit a regular shape. The size of the pores is about 1.5 mm × 1.5 mm. As shown in Fig. 8$a_2$–$d_2$, at the junction, the connection between the two printing wires is good, and there is no delamination or smashing. As shown in Fig. 8$a_3$–$d_3$, in addition to the pre-designed macroporous structure, the scaffolds also have an open-cell structure formed by the removal of the binder, and the micropores are distributed on the walls of the large pores. Since the structure and size of the micropores produced by the binder removal are irregularly distributed, the scaffolds exhibit a broad interconnected distribution in the range of 10-750 um. As shown in Fig. 8$a_4$–$d_4$, the micropores number on the printed silk decreases as $Mg^{2+}$ content increases, indicating that the sintering of the powder is improved as the $Mg^{2+}$ content in the sample increases, which is due to $Mg^{2+}$ replaces part of $Ca^{2+}$ in β-TCP, the particle size of the powder becomes smaller, the degree of activation is improved and the sintering condition of the powder is improved.

## Shrinkage and porosity of sintered $Mg_xCa_{3-x}(PO_4)_2$ scaffolds

Figure 9 shows the shrinkage and porosity of $Mg_xCa_{3-x}(PO_4)_2$ porous scaffolds with different $Mg^{2+}$ contents. The shrinkage and porosity of the scaffolds are affected by $Mg^{2+}$ content. As $Mg^{2+}$ content increases, the shrinkage of the scaffolds gradually increases. At the same time, the porosity of the scaffolds gradually decreases. When $Mg^{2+}$ content was increased to 30 mol%, the shrinkage ratio of the

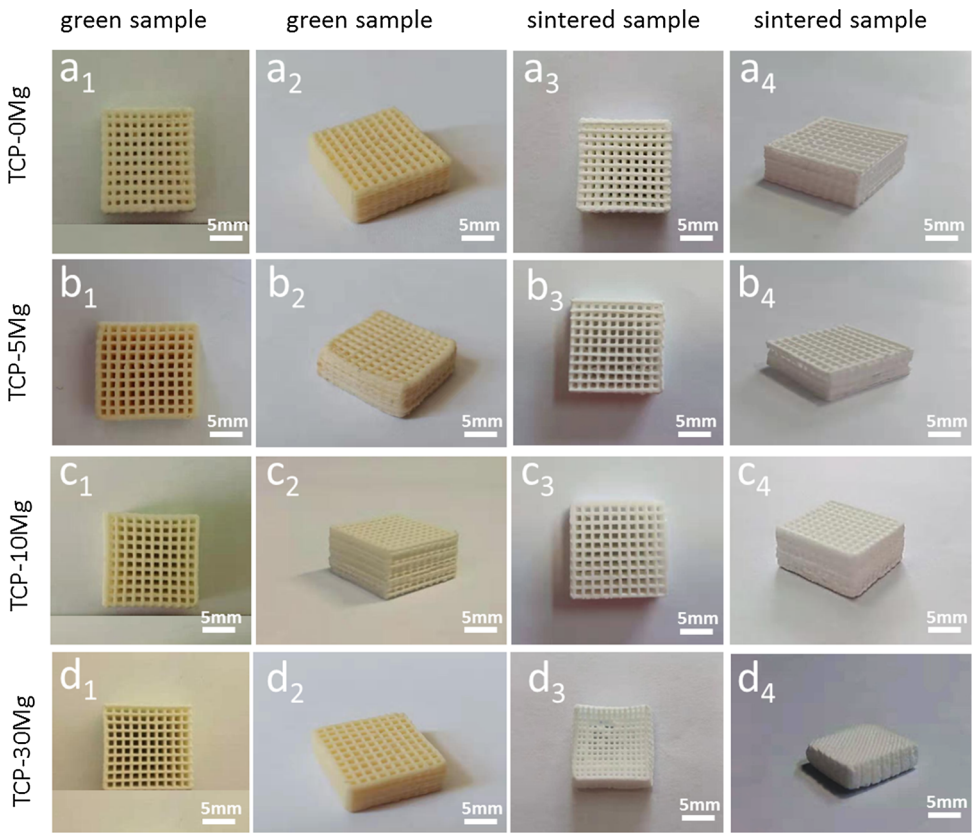


**Figure 7** The macro view of $Mg_xCa_{3-x}(PO_4)_2$ porous scaffolds printed by 3DGP.

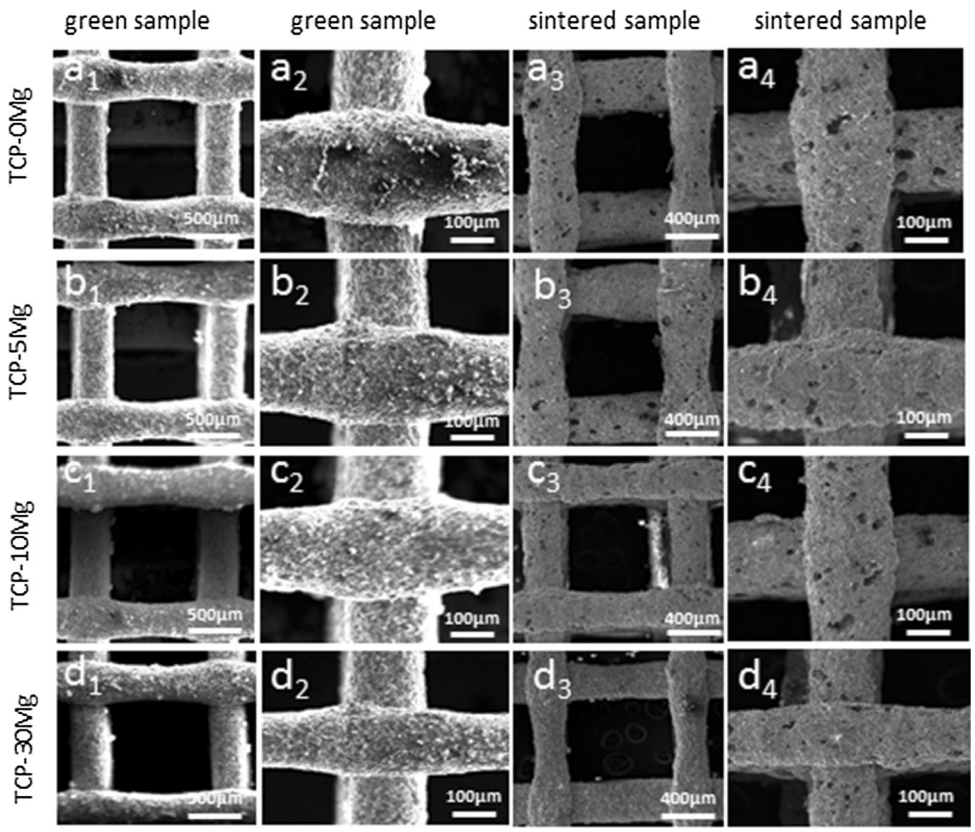


**Figure 8** SEM images of $Mg_xCa_{3-x}(PO_4)_2$ porous scaffolds printed by 3DGP.

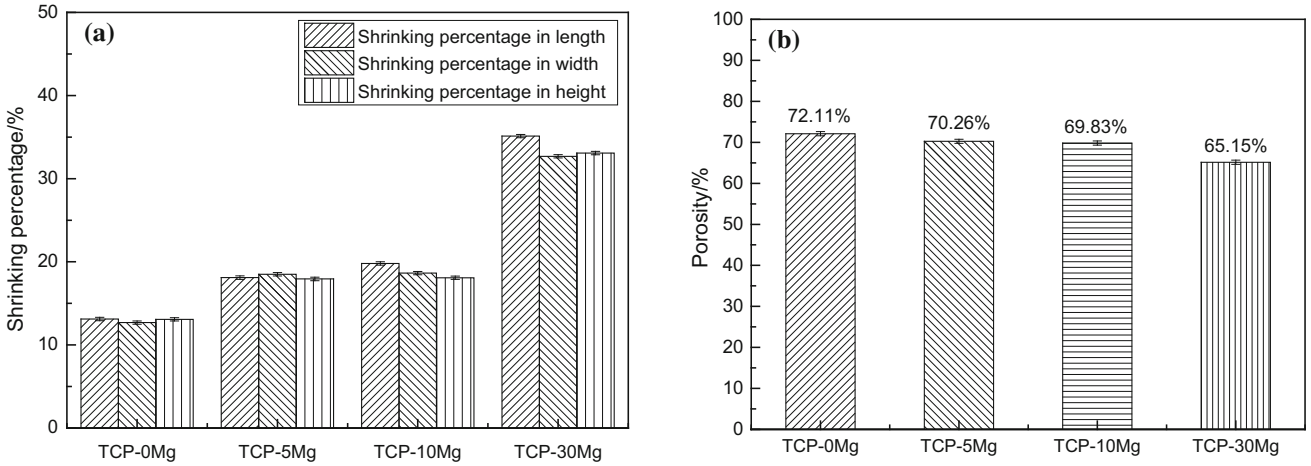


**Figure 9** Shrinkage and porosity of $Mg_xCa_{3-x}(PO_4)_2$ scaffolds.

scaffolds in the three directions of length, width and height was 35.12%, 32.69% and 33.08%, respectively. The shrinkage of TCP-30 Mg scaffolds increased compared to pure β-TCP stent, which is caused by an increase in the electrostatic binding force between Mg–O and Ca–O in the structure and a closer distance between Mg–O and Ca–O in the $Mg_xCa_{3-x}(PO_4)_2$ structure. When the $Mg^{2+}$ content is 0, 5 mol%, 10 mol% and 30 mol.%, the porosity of the sintered stent is 72.11%, 70.26%, 69.83% and 65.15%. Both are higher than the theoretical porosity of 61%. The reason is that the removal of organic matter after sintering makes the pores on the printing yarn increase. With the increase in $Mg^{2+}$ content, the contraction rate of the stent gradually increased. When the $Mg^{2+}$ content increased from 5 to 10 mol%, the shrinkage of the stent increased to a small extent, while the porosity decreased. When the $Mg^{2+}$ content increased to 30 mol%, the shrinkage of the stent significantly decreased, and the porosity also appeared to a large extent decline. In order to further study the effect of $Mg^{2+}$ content on the porosity and shrinkage of the stent, we will conduct a more in-depth study of the role of $Mg^{2+}$ in the next study.

## In vitro degradation of $Mg_xCa_{3-x}(PO_4)_2$ scaffolds

The biodegradable scaffolds provide initial structure and stability for tissue formation. The scaffolds degrade as the tissue is formed, providing space for matrix deposition and tissue growth. The degradation of $Mg_xCa_{3-x}(PO_4)_2$ scaffolds in SBF solution is shown in Fig. 10. Compared to pure β-TCP scaffolds, the degradation of the Mg-doped stent scaffolds is more significant. As $Mg^{2+}$ content increases, the weight loss rate curve of $Mg_xCa_{3-x}(PO_4)_2$ scaffolds for the soaking time is shown in Fig. 11a. There was no significant change in the solubility of pure β-TCP scaffolds throughout the impregnation. At the first week, the quality of Mg-doped stent increased significantly. The dissolution of the porous scaffolds and the precipitation of the apatite phase during the impregnation are simultaneously performed. When the precipitation rate of the apatite phase is faster than the degradation rate of the stent, the mass of the stent will increase. In the second and third weeks, the quality of the stent gradually began to decline. After 3 weeks, the degradation rate of the stent tended to be flat. As the immersion time is extended, the solubility of $Mg_xCa_{3-x}(PO_4)_2$ scaffolds as a whole decreases as $Mg^{2+}$ content increases, which may be caused by a white block phase on the $Mg_xCa_{3-x}(PO_4)_2$ surface.

Figure 11b shows pH change curves of solution in the buffer during the impregnation stage. The pH value decreases with the prolongation of the soaking time. At the beginning of the soaking, the pH value of SBF solution drops sharply. Due to the decomposition of $Mg_xCa_{3-x}(PO_4)_2$ and the precipitation of apatite phase, a large amount of $Ca^{2+}$, $Mg^{2+}$, $PO_4^{3-}$ and $CO_3^{2-}$ exists in the solution. $Ca^{2+}$ and $Mg^{2+}$ are deposited on the surface of the sample, so a large amount of $PO_4^{3-}$ and $CO_3^{2-}$ remains in the SBF solution, causing a sharp drop in the solution pH value. The degradation rate of the material and the deposition rate of the apatite phase change from an unbalanced wave state to an equilibrium state. After

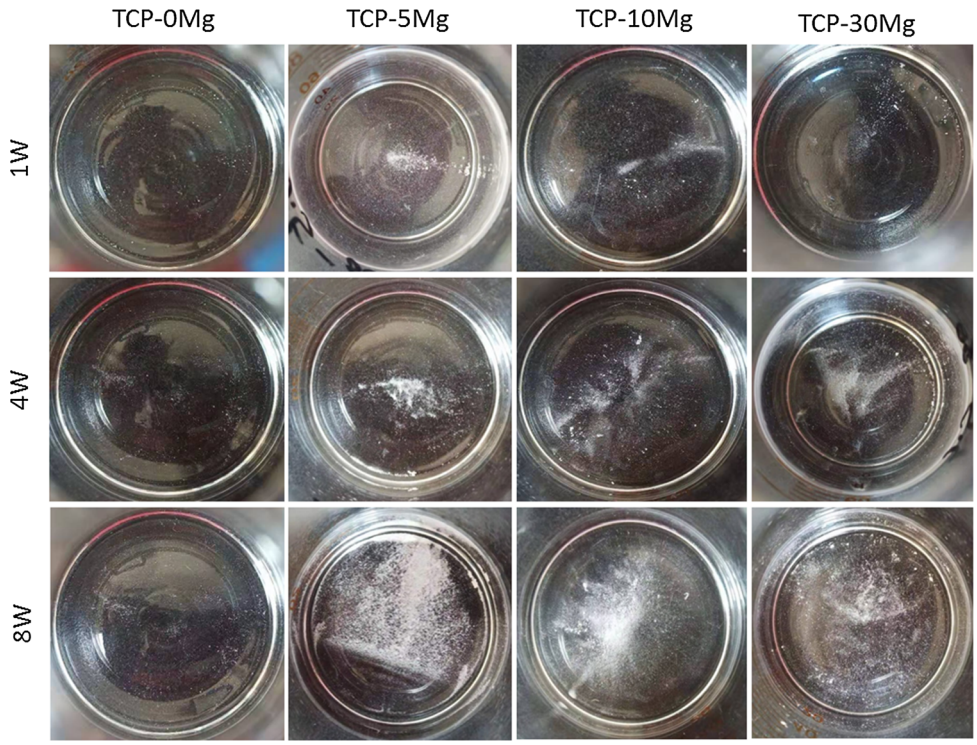


**Figure 10** Degradation of $Mg_xCa_{3-x}(PO_4)_2$ scaffolds in SBF.

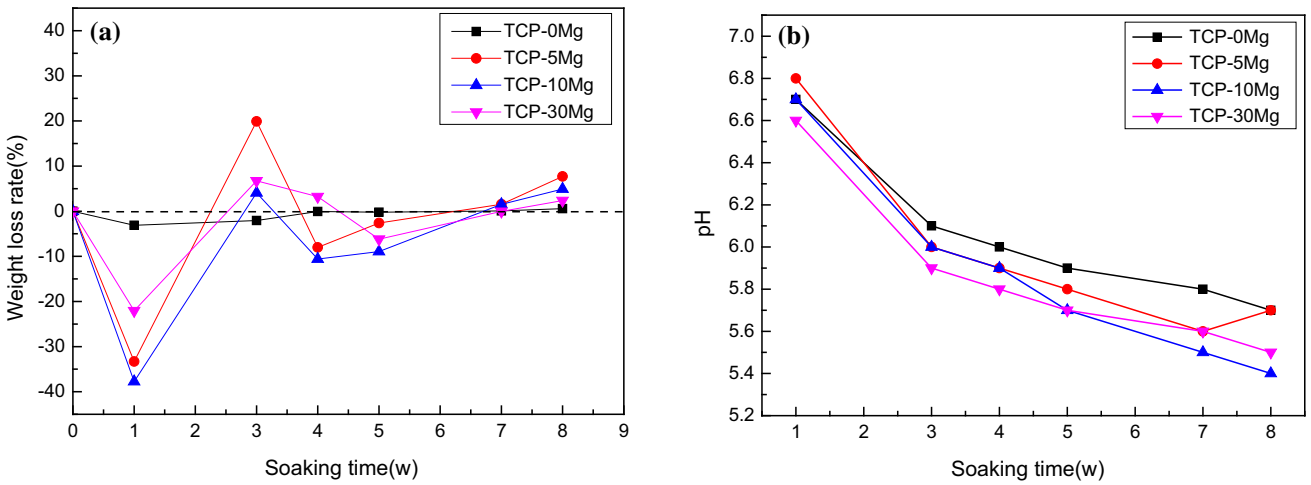


**Figure 11** Weight loss rate of $Mg_xCa_{3-x}(PO_4)_2$scaffolds and pH change of SBF.

soaking for 8 weeks, the solution pH value was about 5.5.

## Compressive strength of $Mg_xCa_{3-x}(PO_4)_2$ scaffolds

The compressive strength curves of $Mg_xCa_{3-x}(PO_4)_2$ scaffolds with different $Mg^{2+}$ contents are shown in Fig. 12. The maximum force in the original chart report generated by the mechanical performance tester is greater than the true maximum force the material can withstand. Due to the presence of large bore passages in the stent, when the powder structure is compressed, the large pores close, creating a more robust structure that provides greater resistance to the applied force. Therefore, the first peak in the resulting graph is considered to be the maximum compressive strength that the stent can withstand. When $Mg^{2+}$ doping content is 0, 5 mol%, 10 mol% and 30 mol%, the compressive strength of the stent is $1.04 \pm 0.01$ MPa, $0.73 \pm 0.17$ MPa, $0.23 \pm 0.01$ MPa and $1.89 \pm 0.21$ MPa, respectively. $Mg^{2+}$ can inhibit

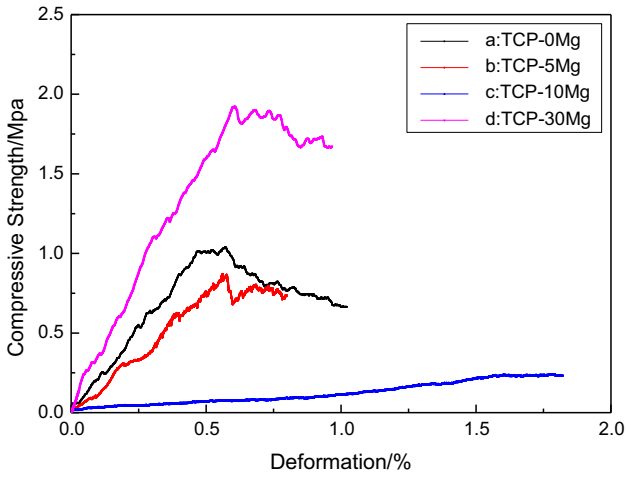


**Figure 12** The compressive strength curve of $Mg_xCa_{3-x}(PO_4)_2$ porous scaffolds printed by 3DGP: **a** TCP-0 Mg [22], **b** TCP-5 Mg, **c** TCP-10 Mg and **d** TCP-30 Mg.

the growth of tricalcium phosphate crystals. The decrease in crystallinity may be the reason for its compressive strength reduction [36]. Previous studies have shown that when magnesium-substituted hydroxyapatite is used to prepare apatite, the incorporation of magnesium reduces the compressive strength of the apatite [37]. As the magnesium ion content increases, the stent shrinks sharply and the porosity decreases, so the stent strength increases. When $Mg^{2+}$ doping amount is 30 mol%, the scaffold has the largest shrinkage rate and the highest strength. The mechanical strength of the scaffolds makes them unsuitable for load-bearing applications. However, they can be used in other applications such as sponge bone, cancellous bone or bone fillers [38–40].

## Conclusions

$Mg_xCa_{3-x}(PO_4)_2$ composite powders were prepared successfully by liquid precipitation method. And the porous $Mg_xCa_{3-x}(PO_4)_2$ composite scaffolds were printed by 3DGP technology. When $Mg^{2+}$ doping content is 30 mol%, the degree of the precursor agglomeration is the smallest, and the particle size of the powder is about 31.93 μm. After TCP-30 Mg scaffolds were sintered at 1100 °C for 3 h, the strength reached a maximum of 1.89 ± 0.21 MPa, and the porosity was 65.15%. In addition, the addition of $Mg^{2+}$ plays a role in regulating the degradation of the scaffolds. Compared to pure β-TCP scaffolds, the degradation of the Mg-doped scaffolds is more significant. And the weight loss rate of the scaffolds decreases with increasing $Mg^{2+}$ content. This approach provides an idea for developing biodegradable, high-strength bio-ceramic scaffolds, which is a huge application prospect in bone defects repairing.

In summary, it was found in the study that $Mg^{2+}$ can replace the $Ca^{2+}$ in β-TCP during the liquid-phase reaction and form a new calcium–magnesium phosphate phase. The addition of $Mg^{2+}$ has a certain regulatory effect on the compressive strength and degradability of the β-TCP scaffold, but no obvious law was found. And a clearer understanding of the specific mechanism of action of $Mg^{2+}$ is lacking. Therefore, the specific mechanism of action of $Mg^{2+}$ will be further explored in the next research work.

## Acknowledgements

This work was supported by the Key Research and Development Projects of the People's Liberation Army (No. BWS17J036).

## Compliance with ethical standards

**Conflict of interest** The authors declare that they have no conflict of interest.

## References

[1] Komaki H, Tanaka T, Chazono M, Kikuchi T (2006) Repair of segmental bone defects in rabbit tibiae using a complex of β-tricalcium phosphate, type I collagen, and fibroblast growth factor-2. Biomaterials 27(29):5118–5126

[2] Yu J, Xia H, Ni QQ (2018) A three-dimensional porous hydroxyapatite nanocomposite scaffold with shape memory effect for bone tissue engineering. J Mater Sci 53(7):4734–4744. https://doi.org/10.1007/s10853-017-1807-x

[3] Gugala Z, Gogolewski S (2002) Healing of critical-size segmental bone defects in the sheep tibiae using bioresorbable polylactide membranes. Injury 33(SUPPL. 2): 71–76

[4] Bose S, Roy M, Bandyopadhyay A (2012) Recent advances in bone tissue engineering scaffolds. Trends Biotechnol 30(10):546–554

[5] Pihlman H, Keränen P, Paakinaho K, Linden J, Hannula M, Manninen IK, Hyttinen J, Manninen M, Laitinen-Vapaavuori O (2018) Novel osteoconductive β-tricalcium phosphate/

poly (L-lactide-co-e-caprolactone) scaffold for bone regeneration: a study in a rabbit calvarial defect. J Mater Sci Mater Med 29(10):156. https://doi.org/10.1007/s10856-018-6159-9

[6] Liu W, Zhai D, Huan Z, Wu C, Chang J (2015) Novel tricalcium silicate/magnesium phosphate composite bone cement having high compressive strength, in vitro bioactivity and cytocompatibility. Acta Biomater 21:217–227

[7] Chen G, Chen N, Wang Q (2019) Fabrication and properties of poly (vinyl alcohol)/β-tricalcium phosphate composite scaffolds via fused deposition modeling for bone tissue engineering. Compos Sci Technol 172:17–28

[8] Jahangir S, Hosseini S, Mostafaei F, Sayahpour FA, Eslaminejad MB (2019) 3D-porous β-tricalcium phosphate–alginate–gelatin scaffold with DMOG delivery promotes angiogenesis and bone formation in rat calvarial defects. J Mater Sci Mater Med 30(1):1. https://doi.org/10.1007/s10856-018-6202-x

[9] Pae HC, Kang JH, Cha JK, Lee JS, Paik JW, Jung UW, Kim BH, Choi SH (2019) 3D-printed polycaprolactone scaffold mixed with β-tricalcium phosphate as a bone regenerative material in rabbit calvarial defects. J Biomed Mater Res Part B Appl Biomater 107(4):1254–1263

[10] Ke D, Dernell W, Bandyopadhyay A, Bose S (2015) Doped tricalcium phosphate scaffolds by thermal decomposition of naphthalene: mechanical properties and in vivo osteogenesis in a rabbit femur model. J Biomed Mater Res Part B Appl Biomater 103(8):1549–1559

[11] Diao J, OuYang J, Deng T, Liu X, Feng Y, Zhao N, Mao C, Wang Y (2018) 3D-Plotted Beta-Tricalcium Phosphate Scaffolds with smaller pore sizes improve in vivo bone regeneration and biomechanical properties in a critical-sized calvarial defect rat model. Adv Healthc Mater 7(17):1800441

[12] Jang HL, Zheng GB, Park J, Kim HD, Baek HR, Lee HK, Lee K, Han HN, Lee CK, Hwang NS, Lee JH, Nam KT (2016) In vitro and in vivo evaluation of whitlockite biocompatibility: comparative study with hydroxyapatite and β-Tricalcium phosphate. Adv Healthc Mater 5(1):128–136

[13] Wopenka B, Pasteris JD (2005) A mineralogical perspective on the apatite in bone. Mater Sci Eng, C 25(2):131–143

[14] Guo X, Long Y, Li W, Dai H (2019) Osteogenic effects of magnesium substitution in nano-structured β-tricalcium phosphate produced by microwave synthesis. J Materi Sci 54(16):11197–11212. https://doi.org/10.1007/s10853-019-03674-7

[15] Mellier C, Fayon F, Boukhechba F, Verron E, Leferrec M, Montavon G, Lesoeur J, Schnitzler V, Massiot D, Janvier P, Gauthier O, Bouler JM, Bujoli B (2015) Design and properties of novel gallium-doped injectable apatitic cements. Acta Biomater 24:322–332

[16] Bracci B, Torricelli P, Panzavolta S, Boanini E, Giardino R, Bigi A (2009) Effect of $Mg^{2+}$, $Sr^{2+}$, and $Mn^{2+}$ on the chemico-physical and in vitro biological properties of calcium phosphate biomimetic coatings. J Inorg Biochem 103(12):1666–1674

[17] Kannan S, Goetz-Neunhoeffer F, Neubauer J, Pina S, Ferreira JMF (2010) Synthesis and structural characterization of strontium-and magnesium-co-substituted β-tricalcium phosphate. Acta Biomater 6(2):571–576

[18] Abrantes JCC, Kaushal A, Pina S, Döbelin N, Bohner M, Ferreira JMF (2016) Influence of Mg-doping, calcium pyrophosphate impurities and cooling rate on the allotropic α↔β-tricalcium phosphate phase transformations. J Eur Ceram Soc 36(3):817–827

[19] Xue W, Dahlquist K, Banerjee A, Bandyopadhyay A, Bose S (2008) Synthesis and characterization of tricalcium phosphate with Zn and Mg based dopants. J Mater Sci Mater Med 19(7):2669–2677. https://doi.org/10.1007/s10856-008-3395-4

[20] Rude RK (1998) Magnesium deficiency: a cause of heterogenous disease in humans. J Bone Miner Res 13(4):749–758

[21] Gallo M, Santoni BLG, Douillard T, Zhang F, Gremillard L, Dolder S, Hofstetter W, Meille S, Bohner M, Chevalier J, Tadier S (2019) Effect of grain orientation and magnesium doping on β-tricalcium phosphate resorption behavior. Acta Biomater 89:391–402

[22] Zhang Y, Shao H, Lin T, Peng J, Wang A, Zhang Z, Wang L, Liu S, Yu X (2019) Effect of Ca/P ratios on porous calcium phosphate salt bioceramic scaffolds for bone engineering by 3D gel-printing method. Ceram Int 45(16):20493–20500

[23] Matsumoto N, Sato K, Yoshida K, Hashimoto K, Toda Y (2009) Preparation and characterization of β-tricalcium phosphate co-doped with monovalent and divalent antibacterial metal ions. Acta Biomater 5(8):3157–3164

[24] Fellah BH, Layrolle P (2009) Sol-gel synthesis and characterization of macroporous calcium phosphate bioceramics containing microporosity. Acta Biomater 5(2):735–742

[25] Guo X, Long Y, Li W, Dai H (2019) Osteogenic effects of magnesium substitution in nano-structured β-tricalcium phosphate produced by microwave synthesis. J Mater Sci 54(16):11197–11212. https://doi.org/10.1007/s10853-019-03674-7

[26] Lian H, Liu X, Meng Z (2019) Enhanced mechanical and osteogenic differentiation performance of hydroxyapatite/zein composite for bone tissue engineering. J Mater Sci 54(1):719–729. https://doi.org/10.1007/s10853-018-2796-0

[27] Cao H, Kuboyama N (2010) A biodegradable porous composite scaffold of PGA/β-TCP for bone tissue engineering. Bone 46(2):386–395

[28] Zairani NAS, Jaafar M, Ahmad N, Razak KA (2016) Fabrication and characterization of porous β-tricalcium phosphate scaffolds coated with alginate. Ceram Int 42(4):5141–5147

[29] Ma Y, Dai H, Huang X, Long Y (2019) 3D printing of bioglass-reinforced β-TCP porous bioceramic scaffolds. J Mater Sci 54(14):10437–10446. https://doi.org/10.1007/s10853-019-03632-3

[30] Yuan J, Zhen P, Zhao H, Chen K, Li X, Gao M, Zhou J, Ma X (2015) The preliminary performance study of the 3D printing of a tricalcium phosphate scaffold for the loading of sustained release anti-tuberculosis drugs. J Mater Sci 50(5):2138–2147. https://doi.org/10.1007/s10853-014-8776-0

[31] Zhang Y, Pan J, Liu WY (2019) Application of 3D printing technology in spinal surgery. J Gannan Med Univ 39(05):537–540

[32] Wen Y, Xun S, Haoye M, Baichuan S, Peng C, Xuejian L, Kaihong Z, Xuan Y, Jiang P, Shibi L (2018) 3D printing porous ceramic scaffolds for bone tissue engineering: a review. Orthop J China 26(14):1306–1310

[33] Kaur G, Pandey OP, Singh K, Homa D, Scott B, Pickrell G (2014) A review of bioactive glasses: their structure, properties, fabrication and apatite formation. J Biomed Mater Res Part A 102(1):254–274

[34] Lichte P, Pape HC, Pufe T, Kobbe P, Fischer H (2011) Scaffolds for bone healing: concepts, materials and evidence. Injury 42(6):569–573

[35] Shao H, He Y, Fu J, He D, Yang X, Xie J, Yao C, Ye J, Xu S, Gou Z (2016) 3D printing magnesium-doped wollastonite/β-TCP bioceramics scaffolds with high strength and adjustable degradation. J Eur Ceram Soc 36(6):1495–1503

[36] Fadeev IV, Shvorneva LI, Barinov SM, Orlovskii VP (2003) Synthesis and structure of magnesium-substituted hydroxyapatite. Inorg Mater 39(9):947–950

[37] Lilley KJ, Gbureck U, Knowles JC, Farrar DF, Barralet JE (2005) Cement from magnesium substituted hydroxyapatite. J Mater Sci Mater Med 16(5):455–460

[38] Seidenstuecker M, Kerr L, Bernstein A, Mayr HO, Suedkamp NP, Gadow R, Krieg P, Latorre SH, Thomann R, Syrowatka F, Esslinger S (2017) 3D powder printed bioglass and β-tricalcium phosphate bone scaffolds. Materials 11(1):13

[39] Xiong Z, Yan Y, Wang S, Zhang R, Zhang C (2002) Fabrication of porous scaffolds for bone tissue engineering via low-temperature deposition. Scr Mater 46(11):771–776

[40] Hernandez CJ, Beaupre GS, Keller TS, Carter DR (2001) The influence of bone volume fraction and ash fraction on bone strength and modulus. Bone 29(1):74–78